

# Investigation of active-region doping on InAs/GaSb long wave infrared detectors\*

Su-Ning Cui(崔苏宁)<sup>1,2</sup>, Dong-Wei Jiang(蒋洞微)<sup>1,2,4</sup>, Ju Sun(孙矩)<sup>1,2</sup>, Qing-Xuan Jia(贾庆轩)<sup>1,2</sup>,  
Nong Li(李农)<sup>1,2</sup>, Xuan Zhang(张璇)<sup>1,2</sup>, Yong Li(李勇)<sup>1,3</sup>, Fa-Ran Chang(常发冉)<sup>1</sup>,  
Guo-Wei Wang(王国伟)<sup>1,2,4,‡</sup>, Ying-Qiang Xu(徐应强)<sup>1,2,4</sup>, and Zhi-Chuan Niu(牛智川)<sup>1,2,4,5,†</sup>

<sup>1</sup>State Key Laboratory for Superlattices and Microstructures, Institute of Semiconductors, Chinese Academy of Sciences, Beijing 100083, China

<sup>2</sup>College of Materials Science and Opto-Electronic Technology, University of Chinese Academy of Sciences, Beijing 100049, China

<sup>3</sup>School of Energy and Environment Science, Key Laboratory of Renewable Energy Advanced Materials and Manufacturing Technology (Ministry of Education), Provincial Key Laboratory of Optoelectronic Information Technology, Yunnan Normal University, Kunming 650092, China

<sup>4</sup>Center of Materials Science and Optoelectronics Engineering, University of Chinese Academy of Sciences, Beijing 100049, China

<sup>5</sup>Beijing Academy of Quantum Information Sciences, Beijing 100193, China

(Received 28 October 2019; revised manuscript received 22 January 2020; accepted manuscript online 18 February 2020)

The eight-band  $k \cdot p$  model is used to establish the energy band structure model of the type-II InAs/GaSb superlattice detectors with a cut-off wavelength of 10.5  $\mu\text{m}$ , and the best composition of M-structure in this type of device is calculated theoretically. In addition, we have also experimented on the devices designed with the best performance to investigate the effect of the active region p-type doping temperature on the quantum efficiency of the device. The results show that the modest active region doping temperature (Be: 760 °C) can improve the quantum efficiency of the device with the best performance, while excessive doping (Be: > 760 °C) is not conducive to improving the photo response. With the best designed structure and an appropriate doping concentration, a maximum quantum efficiency of 45% is achieved with a resistance–area product of 688  $\Omega\cdot\text{cm}^2$ , corresponding to a maximum detectivity of  $7.35 \times 10^{11} \text{ cm} \cdot \text{Hz}^{1/2}/\text{W}$ .

**Keywords:** long-wavelength, barrier design, absorption region doping

**PACS:** 85.60.Gz, 68.65.Cd, 02.70.-c, 72.20.Jv

**DOI:** 10.1088/1674-1056/ab773c

## 1. Introduction

In recent years, the increasing applications of long-wave infrared (LWIR) detectors in numerous fields, especially in ballistic missile defense, remote sensing, and meteorological monitoring, have promoted the research and development of long-wave infrared detectors.<sup>[1]</sup> As the most widely used infrared detector to date, mercury cadmium telluride (MCT) is not a perfect material system due to the intrinsic shortcomings such as the poor uniformity of large area and the difficulty of alloy component adjustment.<sup>[2,3]</sup> After proposed by Sai-Halasz *et al.* in 1997, the InAs/GaSb superlattice with a type-II band gap alignment is considered as a promising alternative to the state-of-the-art MCT technology in the LWIR detection for its various advantages, like the adjustable band gap energy,<sup>[4–6]</sup> the low Auger recombination rate,<sup>[7]</sup> the large electron effective mass,<sup>[8]</sup> and the convenience of material growth and device preparation process.<sup>[9]</sup> In addition to the traditional p–n or p–i–n structure, there are a variety of hetero-junction configurations of antimony-based type-II superlattice that is closely lattice matched to obtain lower dark current density and relatively higher device performance.

There are two most important indicators for measuring

the performance of infrared detectors. One is the dark current density (resistance–area product), and the other is the quantum efficiency (QE). While the dark current density can be reduced by proper band engineering design and passivation process, there are many ways to improve the quantum efficiency, such as increasing the length of the absorption layer<sup>[10]</sup> and reducing the reflectivity of the material surface. Despite the investigations of the LWIR InAs/GaSb superlattice detector have made significant progress, there remains a challenge of how to reduce the dark current without decreasing the quantum efficiency.<sup>[11]</sup> Fortunately, with the presence of barrier structure inserted by a wide bandgap AlSb layer, the contradiction between reducing dark current and improving quantum efficiency is remarkably alleviated by the appropriate superlattice structure design.<sup>[12,13]</sup> Different from other literatures, this paper combines the two optimization methods of performance. First, the best long wave device structure is designed by band simulation. On the basis of this device structure, a series of devices are prepared to vary the doping concentration of beryllium in the absorption region, from which the infrared detection device with low dark current density and high quantum efficiency is obtained.

\*Project supported by the National Key Technology R&D Program of China (Grant No. 2018YFA0209104), the Key R&D Program of Guangdong Province, China (Grant No. 2018B030329001), and the Major Program of the National Natural Science Foundation of China (Grant No. 61790581).

†Corresponding author. E-mail: [zcnui@semi.ac.cn](mailto:zcnui@semi.ac.cn)

‡Corresponding author. E-mail: [wanguguowei@semi.ac.cn](mailto:wanguguowei@semi.ac.cn)

© 2020 Chinese Physical Society and IOP Publishing Ltd

<http://iopscience.iop.org/cpb> <http://cpb.iphy.ac.cn>

In this paper, we first design a LWIR P- $\pi$ -M-N photodetector in terms of energy band. Then, we use the designed structure to carry out the experiment of the absorption region p-type doping with variable temperatures. Finally, we summarize the experiment and obtain the optimum temperature of Be doping in the absorption region.

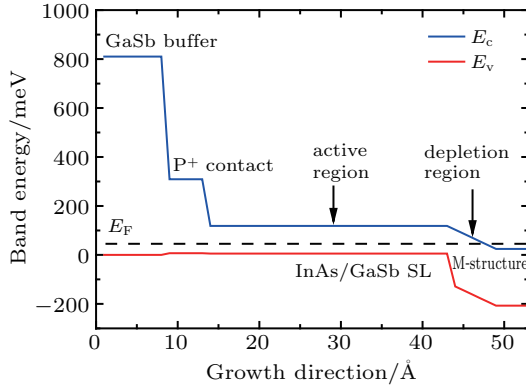


Fig. 1. Schematic diagram of a P- $\pi$ -M-N superlattice photodiode design.

## 2. Theoretical simulation

In this work, we use the M-superlattice composed of InAs/GaSb/AlSb as a barrier layer to reduce the dark current of the LWIR device. In order to get the best LWIR device model, we design the energy bands of superlattice materials in the active layer and the barrier layer, respectively. We use the eight band  $k \cdot p$  method from Ref. [14] to design the band structures using MATLAB software. Figure 2 shows the conduction band and valence band edge energies and corresponding wave functions when the absorption region is configured as 12 ML InAs/7 ML GaSb. By calculation, the band-edge energy difference is about 124 meV, so the theoretical cut-off wavelength is 10  $\mu\text{m}$ . Then, we begin to design the composition of the barrier layer that matches the absorption region. In the M-superlattice structure shown in Fig. 3, the thicknesses of the InAs and AlSb layers are fixed at 18 ML and 5 ML, respectively. When the thickness of the GaSb layer changes from 3 ML to 8 ML, the energy of the conduction band edge increases monotonously from 24.61 meV to 129.56 meV, and the valence band edge increases from  $-207.08$  meV to  $-67.66$  meV. We can see that with the increase of the GaSb layer thickness, the conduction band edge of the barrier region gradually exceeds the absorption region, which will hinder the collection of electrons. At the same time, the upward movement of the valence band edge of the barrier region will weaken the barrier region's blocking effect on the hole diffusion current. Therefore, we use 18/3/5/3 ML InAs/GaSb superlattice configuration to match the absorption region of 12/7 ML InAs/GaSb superlattices with a cut-off wavelength of about 10  $\mu\text{m}$  to obtain "negative offset".<sup>[15]</sup> In this paper, the band edge energies of each region are shown in Table 1

and the zero energy reference point is taken from the top of the GaSb valence band.

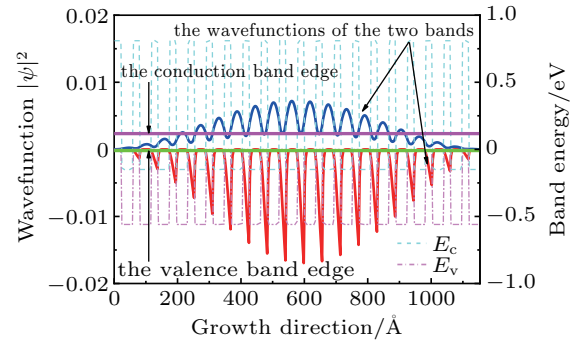


Fig. 2. Simulation result of the active region in terms of band structure.

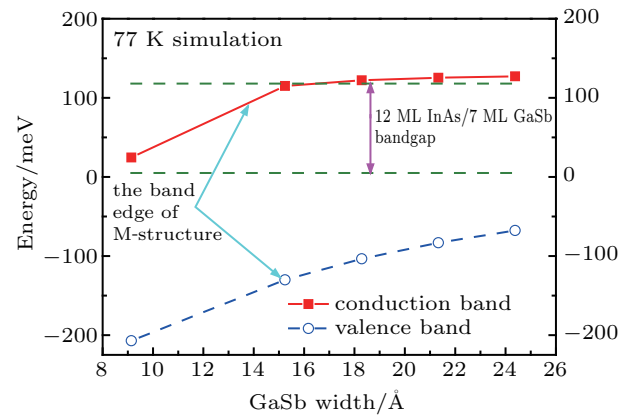


Fig. 3. Calculations of the InAs/GaSb/AlSb M-structure superlattice: 18 ML InAs/ $m$  ML GaSb/5 ML AlSb/ $m$  ML GaSb where  $m = 3, 5, 6, 7, 8$ .

According to the band-edge energy of the device from Table 1, the conduction band edge energy of M-region is lower than that of I-region. Moreover, the valence band edge deviates greatly, which indicates that the device design is in accordance with the theoretical expectation without considering doping in the I-region or slight doping. The profile of the designed device is shown in Fig. 5.

Table 1. Band edge energy of each region of a P- $\pi$ -M-N superlattice device.

Band edge energy	$E_c$ /meV	$E_v$ /meV	$E_g$ /meV	$\lambda/\mu\text{m}$
M-region	24.5	-207	232	5.35
I-region	118.5	5.15	123.6	10.03
P-region	309	7.04	316	3.92
P <sup>+</sup> buffer	810	0	810	1.53

## 3. Experiments

From the expression of detectivity, we can conclude that the effect of quantum efficiency on detectivity is actually greater than that of dark current, as the  $R_0A$  term in the expression has an additional root sign. Therefore, this paper focuses on how to improve the quantum efficiency of LWIR devices by doping the active region. Quantum efficiency reflects the ability of incident photons to convert into photo-current, which is ought to include the optical absorption ability of materials,

the transport of photo-generated carriers, and the collection efficiency of electrodes. Previous literatures have studied the variation of quantum efficiency with doping concentration in the active region on a series of VLWIR photodetectors with a cutoff wavelength of 21  $\mu\text{m}$ .<sup>[11]</sup> Based on the previous experiments, this paper will explore the effect of doping in the active region on long-wave devices with cut-off wavelength of about 10.5  $\mu\text{m}$ .

### 3.1. Quantum efficiency

Assuming that the surface recombination rate is zero, the expression of the total external QE for a p-i-n detector is<sup>[16]</sup>

$$\eta_{\text{Total}} = \eta_n + \eta_{\text{dr}} + \eta_p, \quad (1)$$

and the QEs in n-, depletion-, and p-regions are defined as

$$\eta_n = (1-R) \frac{\alpha L_h}{(\alpha L_h)^2 - 1} \times \left\{ \frac{\alpha L_h - \exp(\alpha x_n) \sinh(x_n/L_h)}{\cos(x_n/L_h)} \right\}, \quad (2)$$

$$\eta_{\text{DR}} = (1-R) \{ \exp(-\alpha x_n) - \exp(-\alpha(x_n + x_{\text{DR}})) \}, \quad (3)$$

$$\eta_p = (1-R) \frac{\alpha L_n}{(\alpha L_n)^2 - 1} \times \left\{ \frac{-\alpha L_n - \exp(\alpha x_p) \sinh(x_p/L_n)}{\cos(x_p/L_n)} + \alpha L_n \right\}. \quad (4)$$

The definitions of the parameters in these formulas can all be found in Ref. [16]. An effective way to improve the QE is to modify the doping type of the active region. In the LWIR device, the thickness of InAs is larger than that of GaSb in one period, unintentionally leaving a residually n-type doping active region. Compared with the p-type doping, the n-type absorption layer is not benefit to the transport of photo-generated carriers because the diffusion length of the holes is less than that of electrons. Therefore, an effective way to improve the QE is to modify the doping type of the active region from n-type to p-type. However, on the other hand, excessive doping will increase the defect density of the material and thus results in a shorter lifetime of the minority carrier, which on the contrary diminishes the QE. Therefore, finding a suitable doping concentration in the active region is a subject worthy of study.

### 3.2. Dark current density

In order to better analyze the dominant dark current mechanism in the devices, we set up the dark current model of the detectors. In general, the dark current in the detector can be divided into bulk dark current and surface leakage current. Among them, the different components of the bulk dark current have analytical expression forms

$$J_{\text{diff}} = n_i^2 \sqrt{ek_B T} \left( \frac{1}{N_D} \sqrt{\frac{\mu_h}{\tau_h}} + \frac{1}{N_A} \sqrt{\frac{\mu_e}{\tau_e}} \right) (e^{eV/k_B T} - 1), \quad (5)$$

$$J_{\text{GR}} = \frac{en_i W}{\tau_{\text{GR}}} \frac{2k_B T}{e(V_B - V)} \sinh\left(-\frac{eV}{2k_B T}\right) f(b), \quad (6)$$

$$J_T = \frac{e^3 E(V) V}{4\pi^2 \hbar^2} \sqrt{\frac{2m_T}{E_g}} \exp\left(-\frac{4\sqrt{2m_T} E_g^3}{3e\hbar E(V)}\right), \quad (7)$$

$$J_{\text{trap}} = \frac{e^2 m_T V M^2 N_t}{8\pi \hbar^3} \exp\left(-\frac{4\sqrt{2m_T} (E_g - E_t)^3}{3e\hbar E(V)}\right). \quad (8)$$

The definition and value of each parameter can be found in many literatures.<sup>[17-19]</sup>

Figure 4 is the experimental fitting curve of the doping concentration corresponding to the doping temperature, from which we can get the corresponding doping concentration of the absorption region under each doping temperature, whose value is used for the latter dark current simulation to illustrate the experimental results.

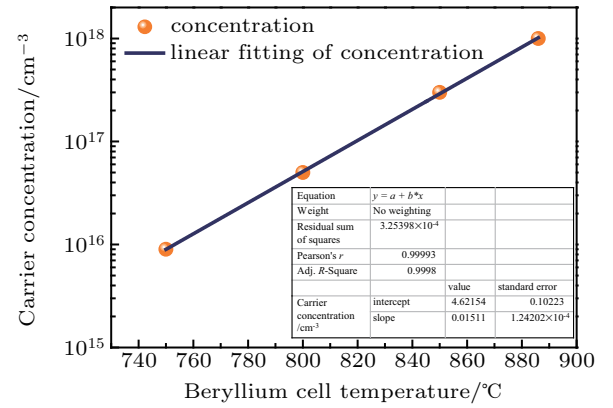


Fig. 4. The relationship between Be doping concentration and temperature.

### 3.3. Experimental design

In this work, we used a solid source Gen II molecular beam epitaxy (MBE) reactor to grow a series of superlattice photodetectors with an active region structure of 12 ML InAs/ 7 ML GaSb (SLs) with a cutoff wavelength of about 10.2  $\mu\text{m}$  on an n-type GaSb (001) substrate. An InSb layer was grown between the InAs and GaSb. The structure consists of a 0.8  $\mu\text{m}$  p<sup>+</sup>-doping GaSb buffer followed by a 0.5  $\mu\text{m}$  InAs/GaSb SLs P<sup>+</sup>-region (Be doping concentration  $1 \times 10^{18} \text{ cm}^{-3}$  in both regions). Then, a 3  $\mu\text{m}$  12 ML InAs/7 ML GaSb SLs active region was grown with different Be doping temperatures (760  $^{\circ}\text{C}$ , 780  $^{\circ}\text{C}$ , 800  $^{\circ}\text{C}$ , 820  $^{\circ}\text{C}$ ). Next, a 0.5  $\mu\text{m}$  18 ML InAs/3 ML GaSb/5 ML AlSb/3 ML GaSb M-structure SLs was grown with a slightly Si doping concentration of  $1 \times 10^{16} \text{ cm}^{-3}$ . Finally, a 20 mm n<sup>+</sup> InAs cap was grown followed by a 0.5  $\mu\text{m}$  N<sup>+</sup>-region M-structure SLs (Be:  $1 \times 10^{18} \text{ cm}^{-3}$ ) with a similar structure of the previous barrier region. Four epitaxial wafers were grown in this experiment and except for the different doping temperatures of Be in the active region, the growth conditions were kept the same. All samples were processed and characterized in

exactly the same way, using standard photo-lithography techniques. In order to suppress the surface leakage current, the surfaces of the all devices were passivated with SiO<sub>2</sub>. Each epitaxial wafer includes three mesa areas of side lengths of 117 μm, 167 μm, and 250 μm.



Fig. 5. A schematic of P- $\pi$ -M-N photodetector.

### 3.4. Experimental result

Figure 6 depicts the dependence of the QE of the four devices on the bias voltage. As the bias voltage changes from positive to negative, the QE rises first and then remains almost unchanged. The figure clearly shows that the QE of all devices tends to be saturated when the reverse bias voltage is 30 mV, indicating that a small bias can help the photo-generated carriers to be basically collected, which verifies the rationality of the device model design described in the previous section. Among the four devices, the one with the active region Be doping temperature 760 °C has the highest QE and the maximum value can reach 44% at -90 mV. Besides, the QE of the devices decreases with the increase of the  $\pi$ -region Be doping temperature. This is mainly because the higher the temperature, the higher the defect density of the material, which leads to the decrease of the minority carrier diffusion length, thus damaging the quantum efficiency.

Figure 7 demonstrates the optical performance characterization results of four groups of LWIR devices with the  $\pi$ -region doping temperature ranging from 760 °C to 820 °C. Figures 7(a) and 7(b) are the absolute spectral responses and quantum efficiencies measured at 77 K. As can be seen from the figure, all four devices have similar absolute spectral response curves and a 100% cut-off wavelength of approxi-

mately 10.5 μm, indicating that the superlattice active regions and M-barrier thicknesses of the four devices are consistent, and the forbidden band gaps are almost the same. All devices are applied with a negative bias of 70 mV. When the Be doping temperature of the active region is 760 °C, the peak responsivity of the device is 2.46 A/W at 7.3 μm, while the external maximum QE is 46% at 5.1 μm, which is close to twice that (only 23%) of the high temperature doping (820 °C). The maximum QEs of the other two devices are 42% and 30%, respectively, and the corresponding  $\pi$ -region Be doping temperatures are 780 °C and 800 °C. The decrease of the QE with the increase of the doping concentration may be attributed to the increase of the defect density. From the analytical expression of quantum efficiency, the QE is related to the diffusion length of minority carriers when the device material and thickness are fixed (i.e.,  $R$ ,  $\alpha$ , and  $x_{n,p}$ ), and the diffusion length of electrons ( $L_n$ ) is larger than that of holes (typical values are 0.55 μm and 0.15 μm, respectively). In addition, through the formula of  $L_n = \sqrt{D_n \tau_n}$ , the diffusion length  $L_n$  is related to the minority carrier lifetime. Generally speaking, the higher the doping concentration is (proportional to the doping temperature), the more effective the composite center is, and the shorter the lifetime of the minority carriers is. Figure 7(c) exhibits the specific detectivity of four devices at 77 K, from which we can obtain a maximum value of  $7.35 \times 10^{11} \text{ cm} \cdot \text{Hz}^{1/2}/\text{W}$  at 7.3 μm. The devices with a  $\pi$ -region doping temperature of 760 °C are superior to the undoped and any other devices with a doping temperature above 760 °C.

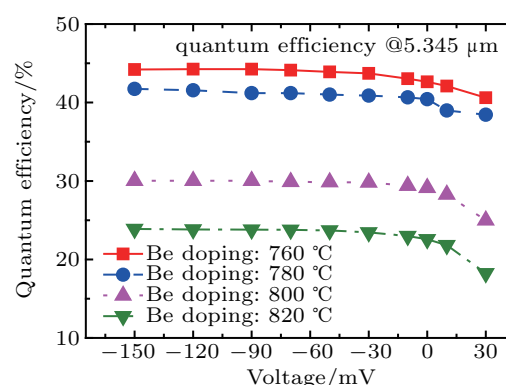


Fig. 6. Quantum efficiency of devices with different  $\pi$ -region doping temperatures under different bias voltages at 5.345 μm wavelength.

The  $J$ - $V$  characteristic reflects the noise level of the detector. Figure 9 shows the dark current density and RA of four devices with variable doping concentration in the active region. The dominant dark current in the detector can be described as the sum of bulk dark current and surface leakage current. In order to suppress the surface leakage current, we passivated the device surface with SiO<sub>2</sub>. To study the effects of the bulk dark current and surface leakage current respectively,

$R_0A$  can be fitted by the following formula:<sup>[19]</sup>

$$\frac{1}{R_0A} = \frac{1}{R_0A_{\text{bulk}}} + \frac{1}{r_{\text{surface}}} \frac{P}{A}, \quad (9)$$

where  $P/A$  is the ratio of perimeter to area of square mesa. Based on the above relationship, we selected a set of devices

to make a curve of  $R_0A$  versus  $P/A$ , as shown in Fig. 8. The slopes of the curves in the figure, which represent  $1/r_{\text{surface}}$ , are quite different from each other, indicating a poor uniformity of the passivation process, which leads to the fact that the dark current does not conform to the simulated behavior with the doping concentration.

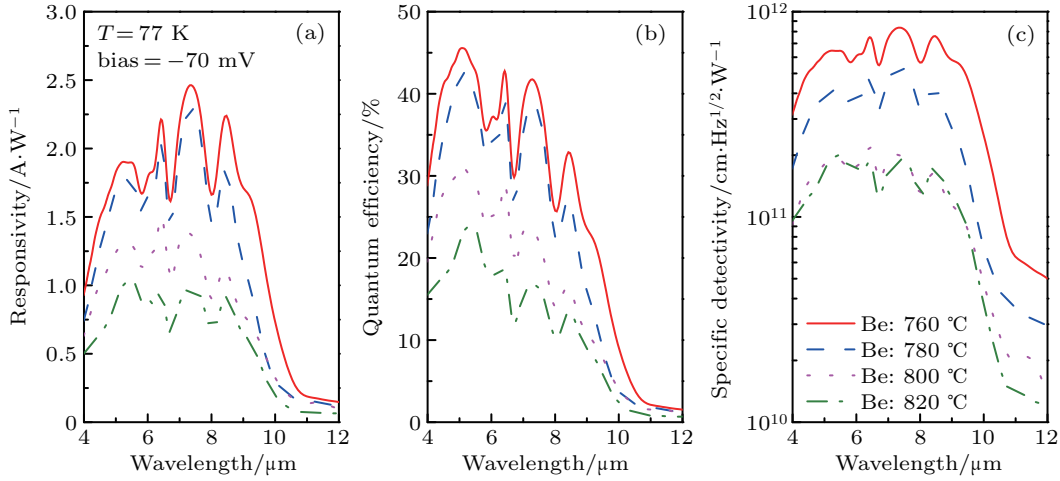


**Fig. 7.** Characterization of optical properties of four groups of devices with  $\pi$ -region doping temperature varying from 760 °C to 820 °C: (a) the absolute responsivity; (b) the QE (%), and (c) the detectivity at 77 K.

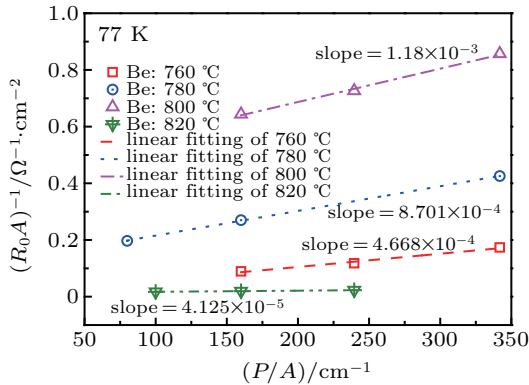


**Fig. 8.** The  $1/R_0A$  as a function of the perimeter to area ratio for LWIR photodetectors at 77 K.

Figure 9 is the curve of the dark current density and resistance–area product of the four devices whose active region is doped at various temperature from 760 °C to 820 °C. Under a bias of  $-100$  mV, the maximum value of  $RA$  of the device with a doping temperature of 760 °C is  $637 \Omega \cdot \text{cm}^2$ , which owns the best dark current characteristic of the four samples. Besides, the device shows diffusion-limitation in a certain reverse voltage range ( $-200$  mV to  $-100$  mV), as the  $RA$  is practically unchanged. Therefore, the samples doped at 760 °C have the best optical response as well as the lowest dark current to achieve the highest detectivity.

In order to explain the behavior of the dark current curve in Fig. 9, we use the aforementioned formulas (5)–(8) to simulate the various components of the bulk dark

current, which is mainly composed of diffusion current, generation–recombination (G–R) current, and tunneling current. As can be seen from the results in Fig. 8, the surface resistivity of the four samples is in the order of  $820 \text{ °C} > 760 \text{ °C} > 780 \text{ °C} > 800 \text{ °C}$ . Figure 10 shows the simulation results of the bulk dark current. Under small reverse bias, the dominant bulk dark current is the G–R current. Although the increase of the doping concentration in the active region will cause the depletion layer to move towards the wide band gap barrier, excessive doping may lead to a significant decrease in G–R lifetime ( $\tau_{\text{GR}}$ ) due to the formation of more defect centers, and thus the total current increases abnormally at 820 °C. As the low surface leakage current of the device counteracts the high G–R current at small reverse bias ( $-200$  mV to  $0$  mV), the total current at 820 °C doping temperature is not lower than that of other samples. The same is true for other devices. Though the samples with doping temperatures of 760 °C and 780 °C have a relatively low G–R dark current, the poor surface passivation makes the total dark current not lower. For the case of applying high reverse bias voltage, the tunneling component plays a dominant role in the bulk dark current, and the sample doped at 820 °C has the largest tunneling dark current, because the  $N_t$  in formula (8) has the largest value. The results of the addition of the surface leakage current and the tunneling current lead to the dark current behavior at high reverse bias in Fig. 9.

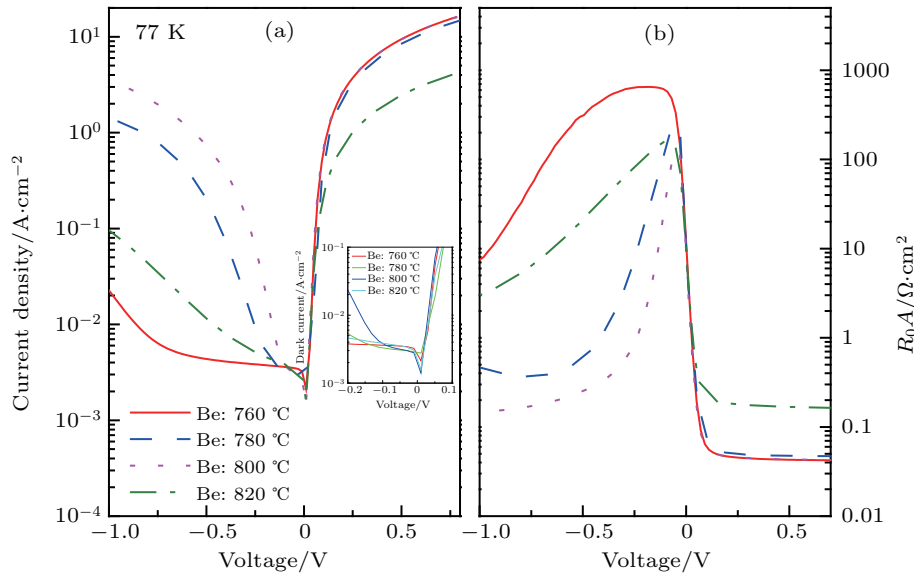


Fig. 9. Characterization of electrical properties of four devices at 77 K: (a) dark current density, (b) the product of resistance and area.

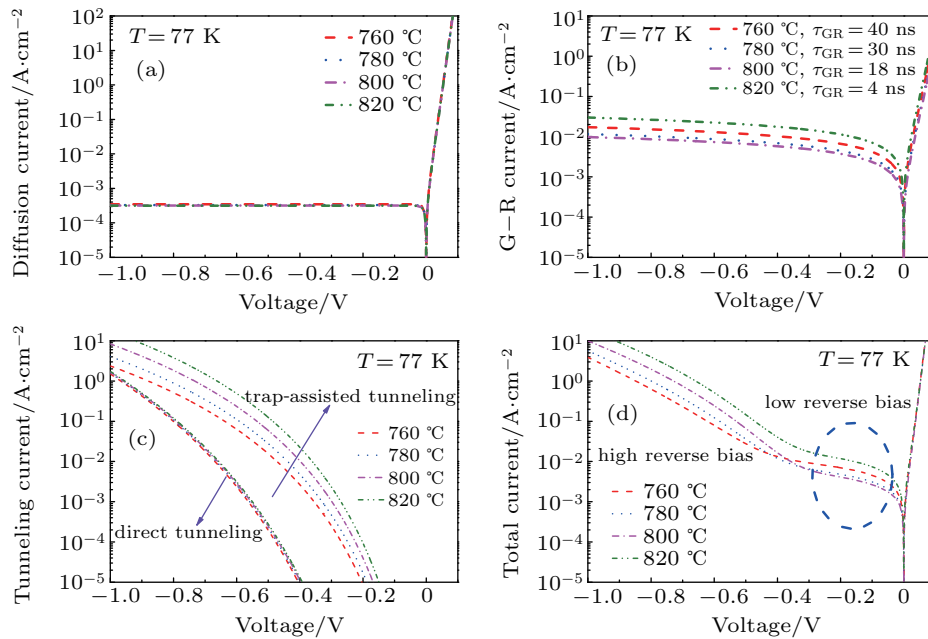


Fig. 10. Behavior of simulated dark current components with doping temperature.

In a few words, the total dark current is the sum of bulk dark current and surface leakage current. In a small reverse bias, the dominant factor of the bulk dark current is the G-R current while tunneling dominates at large reverse voltage.

#### 4. Conclusion

Based on the eight-band  $k \cdot p$  model, a LWIR P- $\pi$ -M-N structure type-II superlattice (T2SL) photodetector with 10.5  $\mu\text{m}$  cut-off wavelength was designed in this paper. By designing a set of devices with different active region doping temperatures, we proved that appropriate doping helps improving the QE, while excessive doping may degrade the performance of the devices in photo response. Unfortunately,

there is no direct evidence that the level of bulk dark current varies with the doping concentration due to the participation of surface dark current. However, the experiments showed that when the doping temperature of the active region is 760  $^{\circ}\text{C}$ , the performance of the LWIR devices is the best. Under 70 mV reverse bias voltage, the quantum efficiency of the device can reach  $45\% \pm 1\%$ , and the maximum detectivity can reach  $7.35 \times 10^{11} \text{ cm} \cdot \text{Hz}^{1/2} / \text{W}$ .

#### References

- [1] Sai-Halasz G A, Tsu R and Esaki L 1977 *Appl. Phys. Lett.* **30** 651
- [2] Andrew H, Manijeh R, Edward H A and Gail J B 2005 *Appl. Phys. Lett.* **87** 151113
- [3] Nguyen B M, Chen G, Hoang M A and Razeghi M 2011 *IEEE J. Quantum Electron.* **47** 686

- [4] Wei Y, Hood A, Yau H, Yazdnapanah V, Razeghi M, Tidrow M Z and Nathan V 2005 *Appl. Phys. Lett.* **86** 091109
- [5] Sullivan G J, Ikhlasi A, Bergman J, DeWames R E, Waldrop J R, Grein C, Flatté M, Mahalingam K, Yang H, Zhong M and Weimer M 2005 *J. Vac. Sci. Technol. B* **23** 1144
- [6] Aifer E H, Jackson E M, Boishin G, Whitman L J, Vurgaftman I, Meyer J R, Culbertson J C and Bennett B R 2003 *Appl. Phys. Lett.* **82** 4411
- [7] Grein C H, Young P M, Flatté M E and Ehrenreich H 1995 *J. Appl. Phys.* **78** 7143
- [8] Smith D L and Mailhot C 1987 *J. Appl. Phys.* **62** 2545
- [9] Martyniuk P, Antoszewski J, Martyniuk M, Faraone L and Rogalski A 2014 *Appl. Phys. Rev.* **1** 041102
- [10] Hood A, Hoffman D, Nguyen B M, Delauney P Y, Michel E and Razeghi M 2006 *Appl. Phys. Lett.* **89** 093506
- [11] Jiang D W, Xiang W, Guo F Y, Hao H Y, Han X, Li X C, Wang G W, Xu Y Q, Yu Q J and Niu Z C 2016 *Appl. Phys. Lett.* **108** 121110
- [12] Nguyen B M, Bogdanov S, Pour S A and Razeghi M 2009 *Appl. Phys. Lett.* **95** 183502
- [13] Nguyen B M, Hoffman D, Delauney P Y and Razeghi M 2007 *Appl. Phys. Lett.* **91** 163511
- [14] Qiao P F, Mou S and Chuang S L 2012 *Opt. Express* **20** 2319
- [15] Bandara S, Baril N, Maloney P, Billman C, Nallon E, Shih T, Pellegrino J and Tidrow M 2013 *Infrared Phys. & Technol.* **59** 18
- [16] Aifer E H, Tischler J G, Warner J H, Vurgaftman I, Bewley W W, Meyer J R, Kim J C and Whitman L J 2006 *Appl. Phys. Lett.* **89** 053519
- [17] Yang Q K, Fuchs F, Schmitz J and Pletschen W 2002 *Appl. Phys. Lett.* **81** 4757
- [18] Nguyen J, Ting Z, Hill J, Soibel A, Keo A and Gunapala D 2009 *Infrared Phys. & Technol.* **52** 317
- [19] Li X C, Jiang D W, Zhang Y, Wang D B, Yu Q J, Liu Tong, Ma H H and Zhao L C 2016 *J. Phys. D* **49** 165105